



Iron Phosphate Nanoparticle Catalyst for Direct Oxidation of Methane into Formaldehyde: Effect of Surface Redox and Acid-Base Properties

Journal:	<i>Catalysis Science & Technology</i>
Manuscript ID	CY-ART-07-2021-001265.R2
Article Type:	Paper
Date Submitted by the Author:	21-Sep-2021
Complete List of Authors:	Matsuda, Aoi; Tokyo Institute of Technology Institute of Innovative Research, Laboratory for Materials and Structures Laboratory, Institute of Innovative Research Tateno, Haruka; Tokyo Institute of Technology Institute of Innovative Research, Laboratory for Materials and Structures Laboratory, Institute of Innovative Research Kamata, Keigo; Tokyo Institute of Technology, Laboratory for Materials and Structures Laboratory, Institute of Innovative Research Hara, Michikazu; Tokyo Institute of Technology Institute of Innovative Research, Laboratory for Materials and Structures Laboratory, Institute of Innovative Research

ARTICLE

Iron Phosphate Nanoparticle Catalyst for Direct Oxidation of Methane into Formaldehyde: Effect of Surface Redox and Acid-Base Properties

Received 00th January 20xx,
Accepted 00th January 20xx

DOI: 10.1039/x0xx00000x

Aoi Matsuda,^a Haruka Tateno,^a Keigo Kamata^{*abc} and Michikazu Hara^{*a}

The effect of various iron phosphate and oxide catalysts on the direct oxidation of methane (CH₄) to formaldehyde (HCHO) with molecular oxygen (O₂) as the sole oxidant was studied using a fixed-bed flow reactor. Five crystalline iron-containing catalysts (FePO₄, Fe₃O₃(PO₄), Fe₄(P₂O₇)₃, Fe₂P₂O₇, and α-Fe₂O₃) with different iron coordination geometries, iron oxidation states, and Fe/P ratios were synthesized by the sol-gel method using malic acid or aspartic acid. The Fe/P molar ratio had a significant effect on the oxidation catalysis; CH₄ conversion increased with the Fe/P molar ratio, although the selectivity to HCHO decreased. Trigonal FePO₄ nanoparticles synthesized by the malic acid-aided method with an Fe/P molar ratio of 1/1 exhibited the highest activity for the selective formation of HCHO among the catalysts tested, including FePO₄ synthesized by a conventional method. Despite the much higher oxidizing ability of Fe₂O₃ than FePO₄, the oxidation of CH₄ using Fe₂O₃ resulted in the formation of only CO₂. In contrast, the temperature-programmed reaction of FePO₄ with CH₄ gave Fe₂P₂O₇ with the formation of HCHO as a primary product, and Fe₂P₂O₇ reacted with O₂ to regenerate FePO₄. Based on mechanistic studies including the catalyst effect, kinetics, pulse-reaction experiments, and IR spectroscopy, the bulk structural change between FePO₄ and Fe₂P₂O₇ is not involved during the catalysis and the surface redox and acid-base properties of FePO₄ are considered to play an important role in CH₄ oxidation with the structure preservation of bulk FePO₄. The combination of redox-active Lewis acidic iron sites and weakly-basic phosphate units likely contributes to the C–H activation of CH₄ and the suppression of complete oxidation to CO₂, respectively.

1. Introduction

Methane (CH₄), a main component of natural gas, has received considerable attention as a key source material due to its abundance around the world including from nonconventional sources (e.g., shale gas, methane hydrates) and its low emission of greenhouse gases such as carbon dioxide (CO₂) and other toxic pollutants when compared to other fossil fuels such as oil and coal.¹ CH₄ has been mainly utilized as an energy source for heating, cooking, transportation, and electricity generation, and its use as a chemical feedstock is limited to less than 10% of total natural-gas production.² CH₄ conversion into commodity chemicals and fuels currently involves indirect routes via synthesis gas (CO + H₂) produced by energy- and capital-intensive reforming processes.³ Therefore, direct catalytic routes to convert CH₄ into useful chemicals and fuels such as

thermocatalytic,^{2,4–8} electrocatalytic,⁹ and plasma- or electric field-assisted¹⁰ oxidative upgrading (oxidative coupling to ethylene (C₂H₄), oxygenation to methanol (CH₃OH) and/or formaldehyde (HCHO), oxidative halogenation) and nonoxidative dehydrogenative aromatization^{11,12} have been extensively investigated by many experimental and theoretical research groups.^{13,14} However, severe reaction conditions are typically required to activate CH₄, which has strong C–H bonds (440 kJ mol⁻¹, *p*K_a 48; ionization potential 12.5 eV), which results in low yield and selectivity toward the desired products due to subsequent reactions (e.g., over-oxidation). In this context, the design and development of heterogeneous catalysts for selective direct CH₄ transformation remain strongly desirable and a challenging subject of research in catalysis. Identification of key factors to selectively obtain target products from mechanistic and conceptual perspectives is thus one of the most promising approaches.

In the field of heterogeneous catalysis, various effective systems based on metal-exchanged zeolites,^{14–18} metal oxides,^{19–22} supported catalysts,^{23–25} and metal organic frameworks^{26,27} have been reported for the direct oxidative upgrading of CH₄ with O₂, H₂O₂, and N₂O as oxidants. Despite the fewer reports than for these materials, several metal phosphates have also attracted much attention as catalysts for the oxidative transformation of CH₄ into C₂ products,^{28–30} halomethanes,^{31–33} and oxygenates.^{34–42} In particular, Otsuka and Wang reported that low-crystallinity FePO₄ with isolated

^a Laboratory for Materials and Structures, Institute of Innovative Research, Tokyo Institute of Technology, 4259 Nagatsuta-cho, Midori-ku, Yokohama, Kanagawa 226-8503, Japan.

^b Japan Science and Technology Agency (JST), Precursory Research for Embryonic Science and Technology (PRESTO), 4-1-8 Honcho, Kawaguchi, Saitama 332-0012, Japan.

^c JST, Core Research for Evolutional Science and Technology (CREST), 4-1-8 Honcho, Kawaguchi, Saitama 332-0012, Japan.

† Footnotes relating to the title and/or authors should appear here.

Electronic Supplementary Information (ESI) available: [details of any supplementary information available should be included here]. See DOI: 10.1039/x0xx00000x

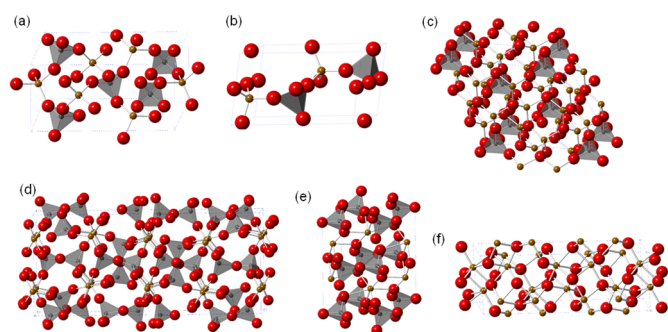


Fig. 1 Structures of (a) trigonal FePO_4 , (b) hexagonal FePO_4 , (c) trigonal $\text{Fe}_3\text{O}_3(\text{PO}_4)$, (d) monoclinic $\text{Fe}_4(\text{P}_2\text{O}_7)_3$, (e) triclinic $\text{Fe}_2\text{P}_2\text{O}_7$, and (f) trigonal Fe_2O_3 . Brown, gray, and red spheres represent Fe, P, and O atoms, respectively.

tetrahedrally coordinated redox-active iron sites is efficient for the selective oxidation of CH_4 into CH_3OH and HCHO with O_2 ,^{34,36} H_2/O_2 ,^{34,39} and N_2O ⁴⁰ as oxidants using a continuous fixed bed flow reactor. Although iron phosphates with various crystal structures have been systematically investigated for the oxidative dehydrogenation of isobutyric acid to methacrylic acid, including the nature of the active phase,⁴³ the effect of the crystal structures of iron phosphates on the direct oxidation of CH_4 has not yet been investigated. On the other hand, the acid properties of metal phosphates also play an important role in the direct oxidation of CH_4 .^{30,42} Gomonaj and Toulhoat reported that the M–O bond strength and the acidity of various crystalline metal phosphates are correlated with the selectivity of CH_4 oxidation toward HCHO using a flow circulation reactor.⁴² We have also reported that monoclinic cerium orthophosphate (CePO_4) with uniform Lewis acid sites could efficiently catalyze the oxidative coupling of CH_4 in an electric field without the need for external heating.^{30,44} However, the role of phosphate units, including surface redox and acid-base properties, is still unclear, because the low specific surface areas of metal phosphates limit detailed characterization of their surfaces.

In the present study, our sol-gel methods for the synthesis of perovskite oxide nanocatalysts^{45–51} are applied to the synthesis of various crystalline iron phosphates and iron oxide, i.e., trigonal FePO_4 , trigonal $\text{Fe}_3\text{O}_3(\text{PO}_4)$, monoclinic $\text{Fe}_4(\text{P}_2\text{O}_7)_3$, triclinic $\text{Fe}_2\text{P}_2\text{O}_7$, and trigonal Fe_2O_3 (Fig. 1), to systematically confirm their intrinsic catalytic performance. We have successfully synthesized various iron-containing catalysts including trigonal FePO_4 nanoparticles ($\text{FePO}_4\text{-MA}$) by the sol-gel method using malic acid (Fig. 2). $\text{FePO}_4\text{-MA}$ exhibits a higher surface area than conventional FePO_4 ³⁴ and higher catalytic activity and selectivity to HCHO than other iron-containing catalysts. The mechanistic studies including the catalyst effect, structure change during redox cycle, surface acid-base property, kinetics, and pulse experiments reveal that redox (in combination with the reversible surface $\text{Fe}^{3+}/\text{Fe}^{2+}$ cycle) and the weakly basic properties of phosphate units would contribute to the promotion of CH_4 oxidation to HCHO and the suppression of complete oxidation to CO_2 , respectively.

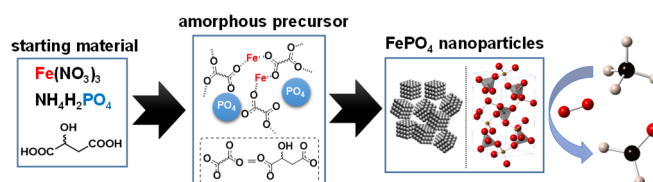


Fig. 2 Schematic representation of the synthesis and catalytic application of FePO_4 nanoparticles by the sol-gel method using malic acid.

2. EXPERIMENTAL

2.1 Instruments.

X-ray diffraction (XRD), inductively coupled plasma-atomic emission spectroscopy (ICP–AES), infrared Fourier transform spectroscopy (FT-IR), thermogravimetry-differential thermal analysis (TG-DTA), H_2 temperature-programmed reduction ($\text{H}_2\text{-TPR}$), nitrogen adsorption-desorption, scanning electron microscopy (SEM), and X-ray photoelectron spectroscopy (XPS) were performed using the apparatuses described in Refs 44–47 and 52. The details are described in the Electronic Supplementary Information (ESI).

2.2 Synthesis of Iron-based Catalysts by the Malic or Aspartic Acid-Aided Method.

Iron-based catalysts such as trigonal FePO_4 , trigonal $\text{Fe}_3\text{O}_3(\text{PO}_4)$, monoclinic $\text{Fe}_4(\text{P}_2\text{O}_7)_3$, and trigonal Fe_2O_3 were synthesized by a sol-gel method using malic acid or aspartic acid.^{45–51} In the case of iron phosphates, the reaction solutions of $\text{Fe}(\text{NO}_3)_3 \cdot 9\text{H}_2\text{O}$, $\text{NH}_4\text{H}_2\text{PO}_4$ (Fe/P ratio: 1/1, 3/1, and 2/3 for FePO_4 , $\text{Fe}_3\text{O}_3(\text{PO}_4)$, $\text{Fe}_4(\text{P}_2\text{O}_7)_3$, respectively), and malic acid (3 equivalents relative to iron contents) were evaporated to dryness to give amorphous precursors. These precursors were calcined in air at the appropriate temperatures (650, 750, and 850 °C for FePO_4 , $\text{Fe}_3\text{O}_3(\text{PO}_4)$, $\text{Fe}_4(\text{P}_2\text{O}_7)_3$, respectively) for 5 h. In the case of Fe_2O_3 , the amorphous precursor prepared by the reaction of $\text{Fe}(\text{OAc})_2$ with aspartic acid (1.5 equivalents relative to iron contents) was calcined at 400 °C for 5 h in air because aspartic acid-aided method has a slight advantage over malic acid-aided method in improving the surface area of SrMnO_3 .⁴⁵ We separately confirmed that Fe_2O_3 could be also synthesized even by using malic acid. $\text{Fe}_2\text{P}_2\text{O}_7$ was prepared by the calcination of $\text{FePO}_4\text{-MA}$ in H_2/Ar (1.5/13.5 mL min^{-1}) at 600 °C for 1 h. The representative synthesis of trigonal $\text{FePO}_4\text{-MA}$ was as follows: $\text{Fe}(\text{NO}_3)_3 \cdot 9\text{H}_2\text{O}$ (6.06 g, 15 mmol), $\text{NH}_4\text{H}_2\text{PO}_4$ (1.73 g, 15 mmol), and DL-malic acid (6.03 g, 45 mmol) were dissolved in water (75 mL) at room temperature. The solution was evaporated to dryness at 80 °C to give a pale-yellow powder as the amorphous precursor. This precursor was calcined at 650 °C for 5 h in air, which yielded 2.13 g (94%) of analytically pure trigonal FePO_4 . Elemental analysis: calcd (%) for FePO_4 : Fe 37.0, P 20.5; found: Fe 37.0, P 20.7.

2.3 Synthesis of FePO_4 ($\text{FePO}_4\text{-CM-550}$, $\text{FePO}_4\text{-CM-600}$) by the Reported Method.

Trigonal FePO_4 was synthesized according to the previously reported procedure.^{34–36} $\text{Fe}(\text{NO}_3)_3 \cdot 9\text{H}_2\text{O}$ (12.1 g, 30 mmol) and

$\text{NH}_4\text{H}_2\text{PO}_4$ (3.45 g, 30 mmol) were dissolved in water (150 mL). The solution was evaporated to dryness at 90 °C, and the resulting pale-yellow powder was dried at 110 °C for 12 h to give a precursor. The precursor was calcined at 550 and 600 °C for 5 h in air to give $\text{FePO}_4\text{-CM-550}$ (a mixture of hexagonal and trigonal phase FePO_4) and $\text{FePO}_4\text{-CM-600}$ (trigonal phase FePO_4), respectively.

2.4 Catalytic oxidation of CH_4 with O_2 .

The oxidation of CH_4 with O_2 over various iron-based catalysts was conducted in a fixed-bed continuous-flow reactor operated at atmospheric pressure. All of the catalysts were pressed into pellets, crushed, and sieved to 32–42 meshes before the reaction. The catalyst (0.05 g) was loaded into a quartz reactor (2 mm inner diameter at the catalyst bed portion) over a plug of quartz wool. A reaction gas containing $\text{CH}_4/\text{O}_2/\text{N}_2$ in a molar ratio of 44/6/50 was used and the total gas flow rate was 16 sccm (i.e., $\text{CH}_4/\text{O}_2/\text{N}_2 = 7/1/8$ sccm). After introduction of the reaction gas flow to the reactor, the reaction temperature was increased from room temperature to 550 °C at a heating rate of ca. 35 °C min^{-1} and then held for 60 min. After the first sampling of the reaction gas, the temperature was decreased by 10 to 450 °C every 60 min with periodic analysis of the reaction gas. The products (CO , CO_2 , CH_3OH , HCHO , CH_3OCH_3 , C_2H_6 , C_2H_4) were analyzed using on-line gas chromatography (Shimadzu GC-8A) with a thermal conductivity detector (TCD) and two packed columns (a mixed column of Porapak-QS/-N and molecular sieves 5A). All of the lines and valves between the reactor exit and the gas chromatograph were heated to 120–130 °C to prevent condensation of the products. Details for the calculations of CH_4 conversion, yield, and selectivity were as follows: CH_4 conversion (%) = carbon of (CO , CO_2 , HCHO)/carbon of input $\text{CH}_4 \times 100$. Yield (%) = carbon of product/carbon of input $\text{CH}_4 \times 100$. Selectivity (%) = yield/ CH_4 conversion $\times 100$. Carbon balance (%) = (carbon of (CO , CO_2 , HCHO) + carbon of output CH_4)/carbon of input $\text{CH}_4 \times 100$. In each case, the carbon balance was in the range of 99.0 \pm 1.6%. The formation of HCHO was also confirmed by trapping the reaction gas into cold CD_3CN solution and analysis of the solution using ^1H nuclear magnetic resonance (NMR) spectroscopy.

2.5 Pulse-reaction experiments for CH_4 oxidation.

The pulse-reaction experiments were performed using a quartz reactor (4 mm inner diameter at the catalyst bed portion) over a plug of quartz wool. The exit gas was directly connected to a gas chromatograph with a TCD (Shimadzu, GC-8A), and HCHO/CO_2 and CO were analyzed using Porapak-QS/-N and 5A molecular sieve columns, respectively. Prior to the pulse-reaction experiments, $\text{FePO}_4\text{-MA}$ (50 mg) was pretreated in a He flow (10 sccm) at 550 °C for 30 min followed by a CH_4 pulse (1 mL) through the catalyst bed at 550 °C five times every 10 min or 60 min.

2.6 Temperature-programmed reaction.

Temperature-programmed reaction profiles were measured using a chemisorption analyzer (BELCAT-A, BEL Japan) equipped with a mass spectrometer (BELMASS, BEL Japan). For the reaction of $\text{FePO}_4\text{-MA}$ with CH_4 , 110 mg of sample was placed in

a quartz cell and pretreated from room temperature to 600 °C at a rate of 20 °C min^{-1} under an O_2 flow (30 mL min^{-1}). After cooling to ca. 50 °C, the sample was heated from 50 °C to 800 °C at a rate of 5 °C min^{-1} under a flow of 5% CH_4/Ar (30 mL min^{-1}). For the reaction of MeOH-adsorbed $\text{FePO}_4\text{-MA}$ and Fe_2O_3 , 100 mg of sample was placed in a quartz cell and then heated from 50 °C to 700 °C at a rate of 5 °C min^{-1} under a He flow (30 mL min^{-1}). The MeOH-adsorbed $\text{FePO}_4\text{-MA}$ and Fe_2O_3 samples were prepared using the Schlenk technique under a dry Ar atmosphere. The dehydrated samples (by heating at 300 °C for 1 h under vacuum) were exposed to saturated MeOH vapor followed by evacuation at 25 °C for 30 min to remove weakly physisorbed MeOH.

3. Result and discussion

3.1 Synthesis and characterization of iron-based catalysts.

The specific surface areas of FePO_4 synthesized by conventional methods are typically low (3–8.5 m^2/g);^{34–36} therefore, the functionalization of FePO_4 by the dispersion of FePO_4 into high-surface area AlPO_4 ($\text{Al}_{1-x}\text{Fe}_x\text{PO}_4$)³⁹ or onto SiO_2 and mesoporous materials^{33,35,36,38} have been reported. However, uncertain active structures of composites and/or the competitive catalytic activity of silica supports themselves for CH_4 oxidation to HCHO make it difficult to evaluate the true nature of FePO_4 , including the structure-activity relationship.^{53,54} Therefore, we focus on the synthesis and catalytic application of FePO_4 nanoparticles with high surface areas because they can lead not only to the functionalization of low-surface-area FePO_4 but also to systematic studies on the intrinsic redox and acid-base properties of various crystalline iron phosphates. Although nano-sized olivine-structured lithium iron phosphate (LiFePO_4) and its precursor have been extensively synthesized as electrode materials,⁵⁵ high-surface-area FePO_4 nanoparticles for the direct catalytic oxidation of CH_4 have not been investigated.

First, iron phosphate and oxide catalyst were synthesized by the sol-gel methods using dicarboxylic acids such as malic acid or aspartic acid.⁴⁵ Trigonal FePO_4 , trigonal $\text{Fe}_3\text{O}_3(\text{PO}_4)$ and monoclinic $\text{Fe}_4(\text{P}_2\text{O}_7)_3$, were also synthesized by the malic acid-aided sol-gel method using $\text{Fe}(\text{NO}_3)_3 \cdot 9\text{H}_2\text{O}$ and $\text{NH}_4\text{H}_2\text{PO}_4$ with molar ratios of $\text{Fe}/\text{P} = 1/1$, $3/1$, and $2/3$, respectively. The local coordination of Fe species is dependent on the crystal structures of iron phosphates. For trigonal FePO_4 with the α -quartz-type structure, each iron and phosphorus atom is tetrahedrally bonded to four oxygen atoms (Fig. 1(a)). In the $\text{Fe}_3\text{O}_3(\text{PO}_4)$ structure, one face of triangular units of distorted trigonal bipyramid Fe^{3+}O_5 species is linked to a PO_4 group (Fig. 1(c)).⁵⁶ $\text{Fe}_4(\text{P}_2\text{O}_7)_3$ consists of Fe_2O_9 clusters of two face-sharing octahedra linked by bent diphosphate P_2O_7 groups (Fig. 1(d)).⁵⁷ Corundum-type $\alpha\text{-Fe}_2\text{O}_3$ (Fig. 1(f)) was synthesized by using aspartic acid without the addition of $\text{NH}_4\text{H}_2\text{PO}_4$.⁵⁸ The synthesis and characterization of trigonal FePO_4 nanoparticles ($\text{FePO}_4\text{-MA}$) synthesized by the sol-gel method using malic acid are described in detail below. The characterization data (XRD and Figs. S1–S5. N_2 sorption) for the other materials are

Table 1. Specific surface area, bulk content, and particle and crystallite size of the iron-based catalysts

Entry	Catalyst	Structure	Iron coordination	S_{BET} ($\text{m}^2 \text{g}^{-1}$)	Crystallite size ^a (nm)	E_a^b (kJ mol^{-1})
1	FePO ₄ -MA	trigonal ($P3_121$, no. 152)	tetrahedral	22	33 (100) 22 (200)	122
2	FePO ₄ -CM-550	hexagonal ($P6_3mc$, no. 186) + trigonal ($P3_121$, no. 152)	tetrahedral	8	–	126
3	FePO ₄ -CM-600	trigonal ($P3_121$, no. 152)	tetrahedral	7	29 (100) 20 (200)	121
4	Fe ₃ O ₃ (PO ₄)	trigonal ($R3m$, no. 160)	distorted trigonal bipyramidal	8	36 (101)	120
5	Fe ₄ (P ₂ O ₇) ₃	monoclinic ($P2_1/n$, no. 14)	octahedral	8	70 (040)	–
6	Fe ₂ O ₃	trigonal ($R-3c$, no.167)	octahedral	34	26 (104)	116

^a Calculated by the XRD peaks. ^b E_a values for the CH₄ oxidation were determined from the Arrhenius plots as shown in Fig. S9.

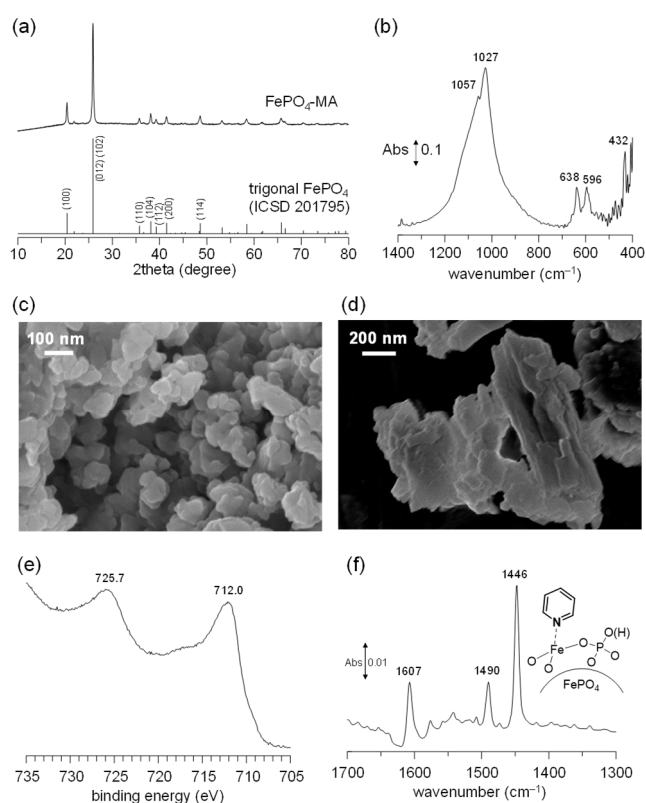


Fig. 3 (a) XRD pattern and (b) IR spectrum for FePO₄-MA. SEM images of (c) FePO₄-MA and (d) FePO₄-CM-600. (e) XPS Fe 2p spectrum for FePO₄-MA. (f) Difference IR spectra for pyridine-adsorbed FePO₄-MA at 25 °C.

summarized in Table 1

Calcination of the amorphous precursor, which was prepared by the reaction of Fe(NO₃)₃·9H₂O with NH₄H₂PO₄ (Fe/P = 1/1) in the presence of 3 equivalents of malic acid relative to Fe, at 650 °C for 5 h in air gave FePO₄-MA. Fig. 3(a) shows the powder X-ray diffraction (XRD) pattern for FePO₄-MA, which was in good agreement with that reported for trigonal FePO₄ (Fig. 1(a), space group $P3_121$).^{43,55} No impurity phases such as iron phosphates, iron oxides, or phosphorous oxides were observed. On the other hand, a mixture of trigonal and

hexagonal FePO₄ (FePO₄-CM-550) was formed by the conventional method (i.e., calcination of a mixture of Fe(NO₃)₃ and NH₄H₂PO₄ at 550 °C),^{36,40} although single-phase trigonal FePO₄ (FePO₄-CM-600) was observed following an increase in the calcination temperature to 600 °C, which is in good agreement with the report that hexagonal FePO₄ (Fig. 1(b), tridymite structure as a polymorph of trigonal FePO₄ with essentially the same connectivity) transitions into trigonal FePO₄ around 500–600 °C.⁵⁹ Elemental analysis using inductively coupled plasma-atomic emission spectroscopy (ICP-AES) showed that the molar ratio of Fe/P was 1/1, which also supports the high purity of the FePO₄-MA phase. The IR spectrum for FePO₄-MA showed a broad band between 1200 and 900 cm⁻¹, two medium bands at 638 and 596 cm⁻¹, and bands around 430 cm⁻¹ that were assignable to symmetric and asymmetric vibrations of P–O bonds, asymmetric vibrations of O–P–O bonds, and symmetric vibrations of O–P–O bonds in trigonal FePO₄, respectively (Fig. 3(b)).⁶⁰ The specific surface area of FePO₄-MA was 22 m² g⁻¹, which is approximately three times larger than that (7 m² g⁻¹) of FePO₄ (FePO₄-CM-600), even though the calcination temperature (650 °C) to produce FePO₄-MA was higher than that (600 °C) for FePO₄-CM-600.

Scanning electron microscopy (SEM) observations of FePO₄-MA showed the formation of spherical nanoparticles with estimated particle sizes of ca. 30–60 nm (Fig. 3(c)), while aggregates of large particles were observed for FePO₄-CM-600 (Fig. 3(d)). These nanoparticle sizes were in reasonable agreement with the grain sizes ($d = 33$ and 22 nm) calculated from the (100) and (200) diffraction lines using Scherrer's equation, respectively. According to the SEM measurement results, the aggregates of FePO₄-CM-600 particles seem to be more compact than FePO₄-MA; thus, the difference in the surface areas between FePO₄-MA and FePO₄-CM-600 would be caused by the state of nanoparticle aggregation. In the case of our sol-gel methods using malic acid, a low-density amorphous precursor (i.e., an amorphous malate salt with the metal cations linked by malate anions) decomposes starting from 400 °C and

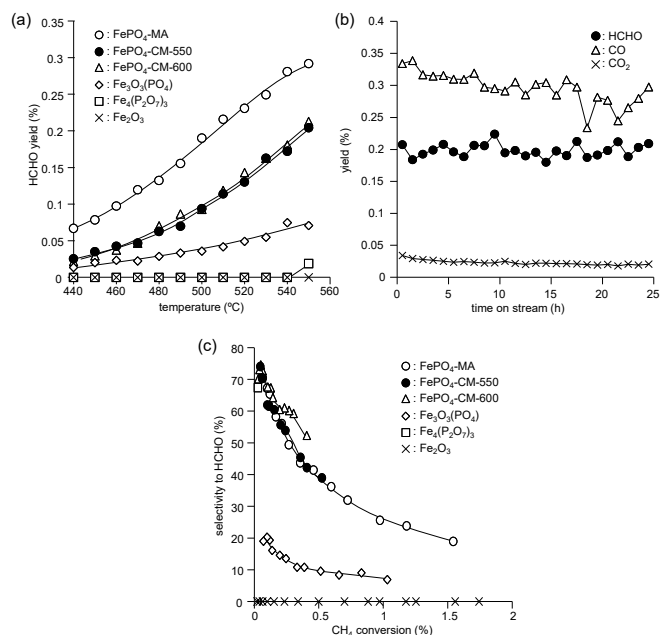


Fig. 4 (a) HCHO yield as a function of reaction temperature over FePO₄-MA, FePO₄-CM-550, FePO₄-CM-600, Fe₃O₃(PO₄), Fe₄(P₂O₇)₃, Fe₂O₃ catalysts. Reaction conditions: catalyst (50 mg), CH₄/O₂/N₂ (7/1/8 sccm), 440–550 °C. (b) Time-on-stream performance of FePO₄-MA catalyst for oxidation of CH₄. Reaction conditions: FePO₄-MA (50 mg), CH₄/O₂/N₂ (7/1/8 sccm), 500 °C. (c) Selectivity toward HCHO as function of CH₄ conversion for oxidation of CH₄ with O₂ over FePO₄-MA, FePO₄-CM-550, FePO₄-CM-600, Fe₃O₃(PO₄), Fe₄(P₂O₇)₃, Fe₂O₃ catalysts.

the formation of the ramified aggregate of crystalline nanoparticles is observed at an appropriate calcination temperature.⁴⁵ The precursor of FePO₄-MA is also amorphous due to the lack of XRD peaks caused by a crystalline material (Fig. S6(a)). On the other hand, the XRD pattern for the FePO₄-CM-600 precursor showed the formation of a complex mixture containing FePO₄·2H₂O and (NH₄)NO₃ (Fig. S6(b)). Such different structures of precursors likely affect the state of nanoparticle aggregation after the calcination.

The X-ray photoelectron spectroscopy (XPS) Fe 2p spectrum of FePO₄-MA showed a peak around 712.0 eV (Fe 2p_{3/2}), which corresponds to Fe³⁺ species, and the binding energy was in good agreement with the reported values for FePO₄ (Fig. 3(e)).⁶¹ The surface atomic Fe/P ratio was estimated to be 0.4, which suggests a phosphate-rich surface structure, which was also supported by infrared (IR) spectroscopy measurements for FePO₄-MA with adsorbed pyridine. The IR spectra of FePO₄-MA with adsorbed pyridine showed a band around 1446 cm⁻¹, which was assigned to pyridine species coordinated with Lewis acid sites, and without a band around 1540 cm⁻¹ that would indicate pyridinium ions bonded to Brønsted acid sites (Fig. 3(f)).⁶² The amount of Lewis acid sites on FePO₄-MA was estimated from the intensities of the band around 1446 cm⁻¹ to be 13 μmol g⁻¹. On the other hand, the acid sites on FePO₄-CM-600 cannot be determined due to the low band intensities, which indicates that the intrinsic surface acid-base properties can be discussed for the first time with the FePO₄-MA

nanoparticles examined in this work. The surface density of exposed Fe cations was calculated to be 0.4 nm⁻² from the Brunauer-Emmett-Teller (BET) surface area, and the amount of Lewis acid sites was much lower than that estimated from the crystal structure (e.g., 2.3 nm⁻² assuming that the (001) plane is a possible surface structure), which is consistent with the phosphate-rich surface structure estimated from the XPS results.

3.2 Oxidation of CH₄ with iron-based catalysts.

The effect of the synthesized iron-based catalysts (FePO₄ (FePO₄-MA, FePO₄-CM-550, and FePO₄-CM-600), Fe₃O₃(PO₄), Fe₄(P₂O₇)₃, and Fe₂O₃) on the oxidation of CH₄ under a CH₄/O₂/N₂ (7/1/8 sccm) flow in the temperature range of 440–550 °C was investigated. In each case, the carbon balance was in the range of 99.0±1.6%. Among the catalysts tested, FePO₄-MA exhibited the highest yield of HCHO (Fig. 4(a)); the HCHO yield at 500 °C decreased in the order of FePO₄-MA (0.19%) > FePO₄-CM-550 and FePO₄-CM-600 (0.09%) > Fe₃O₃(PO₄) (0.04%) > Fe₄(P₂O₇)₃ and Fe₂O₃ (0%). The HCHO yield over FePO₄-MA was 1.4–3.2 times larger than that over FePO₄-CM-550 and FePO₄-CM-600 in the same temperature region, which suggests that the high surface area of FePO₄-MA is effective for the oxidation of CH₄ into HCHO. Three main products, formaldehyde (HCHO), carbon monoxide (CO), and carbon dioxide (CO₂), were formed, whereas other products such as MeOH were not observed. This product distribution is consistent with the previous results obtained using conventional FePO₄ with only O₂,^{34–36} while the formation of MeOH was reported when using H₂-O₂ or N₂O as oxidants.^{34,40} FePO₄-MA also exhibited durability without significant change in the HCHO, CO, and CO₂ yields at 500 °C for 24 h time-on-stream, as shown in Fig. 4(b). The errors during the CH₄ oxidation were estimated to be as follows: selectivity (HCHO: 39.0±5.7%, CO: 56.5±4.9%, CO₂: 4.9±1.1%) and CH₄ conversion: 0.51±0.07%.

Fig. S7 shows the CH₄ conversion and product selectivity as a function of the reaction temperature for the oxidation of CH₄ with various iron-based catalysts. XRD analysis confirmed there was no structural change of the iron-based oxides, and there was no significant difference in the XRD patterns between the fresh and recovered catalysts after CH₄ oxidation (Fig. S8), which indicates that these iron-based catalysts are stable during oxidation and that the CH₄ oxidation ability for each iron-based catalyst originates from its structure. FePO₄-CM-550 (mixed hexagonal/trigonal phase) exhibited a similar HCHO yield and CH₄ conversion to those of FePO₄-CM-600 (single trigonal phase); therefore, the catalytic performance of trigonal FePO₄ is almost the same as that of hexagonal FePO₄.^{37,38} FePO₄-CM-600 was thus used as a conventional FePO₄ counterpart for subsequent experiments. Fig. 4(c) shows the HCHO selectivity against the CH₄ conversion with the various iron-based catalysts. The Fe/P ratio had a significant effect on the CH₄ conversion and selectivity toward HCHO. The CH₄ conversion of Fe₂O₃ without PO₄³⁻ was much higher than the other iron phosphates; however, only the formation of CO₂ was observed. Fe₄(P₂O₇)₃ with a low Fe/P ratio (i.e., Fe/P = 2/3) was almost inactive toward CH₄ oxidation, whereas Fe₃O₃(PO₄) with a high Fe/P

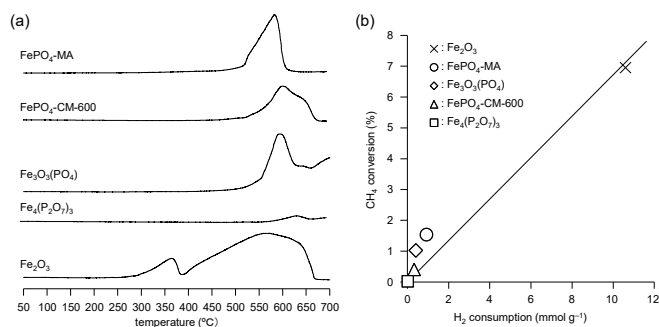


Fig. 5 (a) H₂-TPR profiles for various iron-based catalysts. (b) CH₄ conversion as function of H₂ consumption. CH₄ conversion was determined from CH₄ oxidation at 550 °C under the conditions in Fig. S7. H₂ consumption was estimated from H₂-TPR profiles measured below 550 °C.

ratio of 3/1 exhibited high CH₄ conversion, although its selectivity toward HCHO was low (7–20%). On the other hand, FePO₄ with a molar Fe/P ratio of 1/1 was the most effective among the iron-based catalysts tested for the direct oxidation of CH₄ to HCHO. There was no significant difference in the selectivity-conversion relationship between FePO₄-MA and FePO₄-CM-600, which suggests that the intrinsic nature of the trigonal FePO₄ catalyst is not affected by the particle size. The present space time yield at 550 °C (1.1 mmol_{HCHO} g⁻¹ h⁻¹) of FePO₄-MA was higher than that of conventional FePO₄ (3.8 × 10⁻¹ mmol_{HCHO} g⁻¹ h⁻¹)³⁵ but lower than that of 60 wt% FePO₄/MCM-41 (2.1 mmol_{HCHO} g⁻¹ h⁻¹).³⁵

3.3 Oxidizing ability of iron-based catalysts.

The C–H activation ability of catalyst at lower temperatures is an important factor to selectively promote direct CH₄ oxidation to oxygenates. To investigate the oxidizing ability of iron-based catalysts, H₂-temperature-programmed reduction (TPR) profiles were measured from 50 to 700 °C (Fig. 5(a)). The reduction of Fe₂O₃ began around 270 °C, and two reduction peaks at 350 and 550 °C were attributed to the Fe₂O₃ to Fe₃O₄ and Fe₃O₄ to Fe transitions, respectively. On the other hand, the iron phosphates were reduced at higher temperatures (starting from ca. 450 °C) than Fe₂O₃. The H₂ consumption estimated from the H₂-TPR profiles below 550 °C decreased in the order of Fe₂O₃ (1.06 × 10¹ mmol g⁻¹) >> FePO₄-MA (9.28 × 10⁻¹ mmol g⁻¹) > Fe₃O₄(PO₄) (4.03 × 10⁻¹ mmol g⁻¹) > FePO₄-CM-600 (3.25 × 10⁻¹ mmol g⁻¹) > Fe₄(P₂O₇)₃ (5.00 × 10⁻³ mmol g⁻¹), which is in good agreement with the order of CH₄ conversion at 550 °C (Fe₂O₃ (6.95%) >> FePO₄-MA (1.54%) > Fe₃O₄(PO₄) (1.03%) > FePO₄-CM (0.41%) > Fe₄(P₂O₇)₃ (0.03%)) (Figs. 5(b) and S9). In addition, the activation energy of Fe₂O₃ for CH₄ conversion was 116 kJ mol⁻¹ and lower than those (120–126 kJ mol⁻¹) of the iron phosphate catalysts (Table 1 and Fig. S9).

The structural changes of the iron-based catalysts during the redox reactions were examined next by thermogravimetric-differential thermal analysis (TG-DTA) and XRD analyses. In the TG-DTA profiles under the reductive conditions (H₂/N₂ 10/90, v/v) (Figs. S1(a)–S5(a)), endothermic peaks attributable to the desorption of water was observed below ca. 200 °C followed by

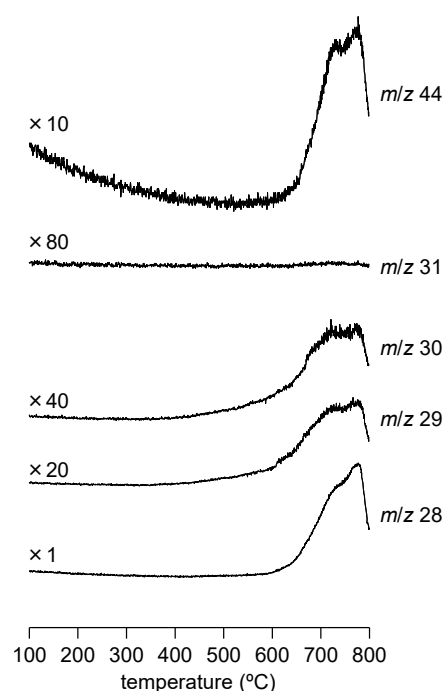


Fig. 6 Mass spectra obtained during the temperature-programmed reaction measurement using FePO₄ in stream of reaction gas mixture composed of CH₄/Ar (5/95, v/v).

reduction of the catalysts in the temperature region of 350–600 °C. The reduction temperatures were in good agreement with the H₂-TPR results. The reduction temperature for high-surface-area FePO₄-MA decreased compared with FePO₄-CM-600 due to the reduced diffusion resistance.⁴⁷ In the case of trigonal FePO₄ (i.e., FePO₄-MA and FePO₄-CM-600), exothermic peaks were observed with a weight loss around 550 °C, and the XRD patterns for the recovered samples were in good agreement with that reported for triclinic Fe₂P₂O₇ composed of distorted Fe²⁺O₆ octahedra and P₂O₇⁴⁻ units (Fig. 1(e)).⁶³ The structural change from FePO₄ to Fe₂P₂O₇ occurs directly without the formation of intermediate phases, as confirmed by the XRD results (Fig. S10). The TG-DTA profiles for the Fe₂P₂O₇ samples under oxidative conditions (O₂ flow) has exothermic peaks with a weight gain around 410 and 620 °C, and the XRD patterns for trigonal FePO₄ were observed again after the treatment at 650 °C in O₂ (Fig. S11). The XRD pattern for the reoxidized sample at 500 °C was close to that for α-Fe₃(P₂O₇)₂, which has been proposed as an active phase in the oxidative dehydrogenation of isobutyric acid.⁶⁴ These results suggest a reversible structural change between FePO₄ and Fe₂P₂O₇ during the redox cycles, according to the possible scheme shown in Fig. S12.⁴³ Although a reversible redox cycle between Fe₂O₃ and Fe was also observed (Fig. S5), Fe₃O₄(PO₄) was irreversibly changed to Fe and Fe₂O₃ under reductive and oxidative conditions, respectively (Fig. S2), and Fe₄(P₂O₇)₃ was not significantly changed during the redox conditions (Fig. S3).

The reactivity of FePO₄-MA with CH₄ instead of H₂ was investigated using temperature-programmed reaction measurements in a stream of a reaction gas mixture composed of CH₄/Ar (5/95, v/v), and the formation of products was

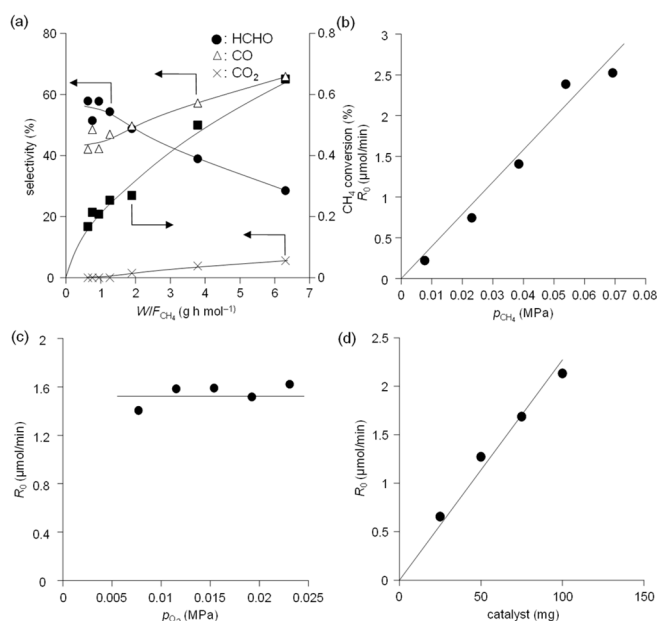


Fig. 7. (a) Effect of W/F_{CH_4} on product selectivity and CH_4 conversion. Effect of partial pressure of (b) CH_4 , (c) O_2 , and (d) catalyst amount on reaction rate. Reaction conditions for (a): $\text{FePO}_4\text{-MA}$ (50 mg), $\text{CH}_4/\text{O}_2/\text{N}_2$ (5:1:7 molar ratio; total 7.8–78 sccm), reaction temperature (500 °C). Reaction conditions for (b): $\text{FePO}_4\text{-MA}$ (50 mg), $\text{CH}_4/\text{O}_2/\text{N}_2$ (1–9/1/11–3 sccm; total 13 sccm), reaction temperature (500 °C). Reaction conditions for (c): $\text{FePO}_4\text{-MA}$ (50 mg), $\text{CH}_4/\text{O}_2/\text{N}_2$ (5/1–3/7–5 sccm; total 13 sccm), reaction temperature (500 °C). Reaction conditions for (d): $\text{FePO}_4\text{-MA}$ (25–100 mg), $\text{CH}_4/\text{O}_2/\text{N}_2$ (5/1/7 sccm; total 13 sccm), reaction temperature (500 °C).

monitored using mass spectrometry (Fig. 6). The formation of CH_3OH (i.e., the signal at m/z 31) was not observed throughout the reaction, which is in good agreement with the catalytic oxidation of CH_4 under steady-state conditions, as shown in Figs. 4 and S7.^{34–36} The signal intensities at m/z 30 and 29 ascribed to HCHO gradually increased from ca. 400 °C and reached a maximum around 700 °C. On the other hand, the signal intensities at m/z 44 and 28 due to CO_2 and CO, respectively, began to increase around 600 °C. In addition, the XRD pattern for the recovered $\text{FePO}_4\text{-MA}$ after the reaction was in good agreement with the trigonal $\text{Fe}_2\text{P}_2\text{O}_7$ structure (Fig. S13). These results indicate that $\text{FePO}_4\text{-MA}$ reacts with CH_4 directly to give HCHO at the initial stage followed by the successive formation of CO and CO_2 with an increase in the reaction temperature, and $\text{Fe}_2\text{P}_2\text{O}_7$ is formed as the final product by the reaction of FePO_4 , even with CH_4 . In this case, phosphate and Fe^{3+} probably act as proton acceptors (also as oxygen donors) and electron acceptors, respectively, and the C–H activation of CH_4 can be formally regarded as a proton-coupled electron transfer (PCET).⁶⁵ Isolated metal oxide cluster ions have been reported to abstract a hydrogen atom from CH_4 by means of PCET on the basis of experimental and computational studies.^{66,67} Therefore, such a mild C–H activation mode of FePO_4 may contribute to the formation of HCHO as a primary product. The effect of contact time (W/F_{CH_4}) on the CH_4 conversion and selectivity toward each

product was investigated by changing the flow rate while maintaining the catalyst loading (50 mg) and reaction temperature (500 °C). Fig. 7(a) shows that the selectivity toward HCHO decreased with an increase in W/F_{CH_4} , while the CH_4 conversion and selectivity toward CO and CO_2 increased, which again indicates that HCHO is the primary product, and CO and CO_2 are formed by the subsequent oxidation of HCHO (eqn (1)). Such a dependence has been reported for the conventional FePO_4 catalyst.³⁴



The reversible structural change between FePO_4 and $\text{Fe}_2\text{P}_2\text{O}_7$ during the reaction of FePO_4 with CH_4 and O_2 indicates that oxygen atoms in the phosphate groups are involved in the activation of CH_4 . Although $\text{Fe}_2\text{P}_2\text{O}_7$ is inactive for the direct oxidation of CH_4 with O_2 in the presence of H_2 or with N_2O ,^{34,40} its catalytic activity for CH_4 oxidation with only O_2 has not been investigated. CH_4 oxidation using $\text{Fe}_2\text{P}_2\text{O}_7$ prepared by the reduction of $\text{FePO}_4\text{-MA}$ with H_2 was investigated to confirm the possible involvement of this redox cycle between FePO_4 and $\text{Fe}_2\text{P}_2\text{O}_7$ (Fig. S14). Despite the lack of a significant difference in CH_4 conversion between $\text{FePO}_4\text{-MA}$ and $\text{Fe}_2\text{P}_2\text{O}_7$ under the present conditions, $\text{Fe}_2\text{P}_2\text{O}_7$ exhibited much lower selectivity toward HCHO than $\text{FePO}_4\text{-MA}$. In addition, XRD analysis of the recovered catalyst after oxidation indicated that the trigonal phase is not completely recovered because the reoxidation of $\text{Fe}_2\text{P}_2\text{O}_7$ into FePO_4 requires a temperature of ≥ 620 °C according to the TG-DTA analysis. The surface oxidation state for iron species of the recovered $\text{FePO}_4\text{-MA}$ catalyst was almost the same as that of a fresh catalyst (Fig. S15). Therefore, $\text{Fe}_2\text{P}_2\text{O}_7$ is not involved during the present oxidation process and is intrinsically less effective than FePO_4 for the oxidation of CH_4 with O_2 .

Kinetic studies on CH_4 oxidation over $\text{FePO}_4\text{-MA}$ at 500 °C were performed to investigate the reaction mechanism. The dependence of the reaction rate (i.e., CH_4 conversion) on the partial pressures of CH_4 (P_{CH_4}) and O_2 (P_{O_2}), and the catalyst loading of $\text{FePO}_4\text{-MA}$ are shown in Figs. 7(b–d). A first-order dependence of the reaction rates on P_{CH_4} and catalyst loading, and a zero-order dependence of the reaction rates on P_{O_2} were observed, which was in good agreement with the results for conventional FePO_4 .³⁴ There was no significant structural difference between the fresh and recovered $\text{FePO}_4\text{-MA}$ catalyst after oxidation; therefore, these kinetic results indicate two possibilities: (i) the surface oxygen species generated from O_2 and FePO_4 react with CH_4 to yield products followed by fast replenishment of the surface oxygen species as proposed by Wang and Otsuka (Fig. S16),^{34,36} or (ii) FePO_4 itself (i.e., phosphate unit) reacts with CH_4 followed by rapid reoxidation to FePO_4 .

Pulse reaction experiments for $\text{FePO}_4\text{-MA}$ pretreated in He at 550 °C were conducted to investigate the possible mechanism in more detail. When the CH_4 pulse (without O_2) was passed through the catalyst bed five times at 550 °C at 10 min intervals, HCHO and CO were formed and no significant amount of CO_2

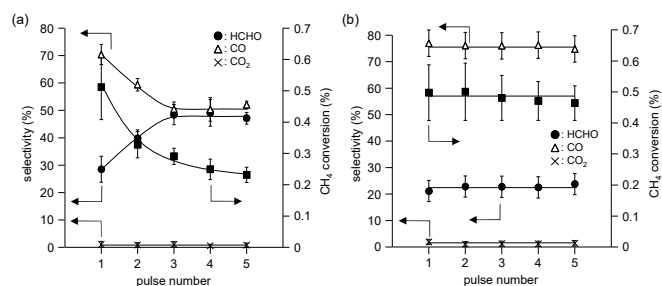


Fig. 8 Plots of product selectivity and CH₄ conversion as function of pulse number for pulse reaction experiments on oxidation of CH₄ with FePO₄-MA. The intervals between each pulse were (a) 10 min and (b) 60 min. Reaction conditions: FePO₄-MA (50 mg), He (10 sccm), CH₄ pulse (1 mL), reaction temperature (550 °C).

was detected. The total yields gradually decreased with an increase in the pulse number, and the selectivity toward HCHO increased slightly (Fig. 8(a)). The molar ratio of Fe species used for oxidation relative to the surface Fe species (determined by pyridine-adsorbed IR spectroscopy) was estimated to be 4–6, considering the number of electrons for each oxidation (i.e., four-, six-, and eight-electron oxidation of CH₄ into HCHO, CO, and CO₂, respectively) and Fe³⁺/Fe²⁺ redox reaction, which indicates that a few surface layers of FePO₄-MA react with CH₄. There was no significant difference in the XRD patterns or IR spectra between the fresh and recovered catalyst after the pulse experiment (Fig. S17), which indicates that CH₄ oxidation most likely occurs on the FePO₄ surface. We carried out the pulse reaction experiments by changing the intervals between each pulse from 10 min to 60 min (Fig. 8(b)). In the case of the pulse experiments at 60 min intervals, the CH₄ conversion and selectivity to HCHO and CO did not change with an increase in the pulse number in contrast to the pulse experiment at 10 min intervals, which indicates the possible migration of surface oxygen vacancies to the bulk of FePO₄-MA. There was no significant difference in the XPS spectra between fresh and recovered FePO₄-MA after the pulse experiments (Fig. S15), also supporting this idea.

3.4 Acid-base properties of iron-based catalysts.

Although Fe₂O₃ had much higher oxidizing ability at lower temperature than FePO₄ on the basis of H₂-TPR and TG-DTA analyses, FePO₄ gave HCHO selectively whereas Fe₂O₃ gave only CO₂ in the same CH₄ conversion region, as shown in Fig. 9; therefore, the significant difference in selectivity cannot be simply explained by the oxidizing ability of the iron-based catalysts. We have recently reported that the unique acid-base properties of metal phosphates result in high catalytic performance not only for chemoselective acetalization, but also for oxidative coupling of CH₄, in sharp contrast to metal oxides.^{30,44} Therefore, the difference in the surface acid-base properties between FePO₄-MA and Fe₂O₃ is also critical to determine the selectivity for CH₄ oxidation. The acid-base properties of FePO₄-MA and Fe₂O₃ were evaluated using IR spectroscopy for samples with adsorbed probe molecules. IR spectra for pyridine-adsorbed FePO₄-MA and Fe₂O₃ indicated that both FePO₄-MA and Fe₂O₃ have only Lewis acid sites (Figs. 3(f) and S18), and the amounts of Lewis acid sites on FePO₄-MA

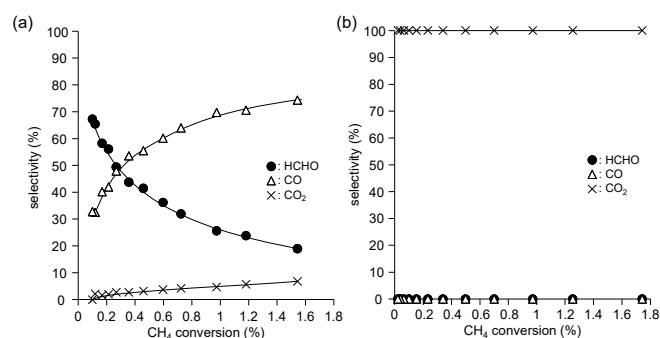


Fig. 9 Product selectivity as function of CH₄ conversion with O₂ over the (a) FePO₄-MA and (b) Fe₂O₃ catalysts. Reaction conditions: catalyst (50 mg), CH₄/O₂/N₂ (7/1/8 sccm), reaction temperature ((a) 440–550 °C and (b) 280–390 °C).

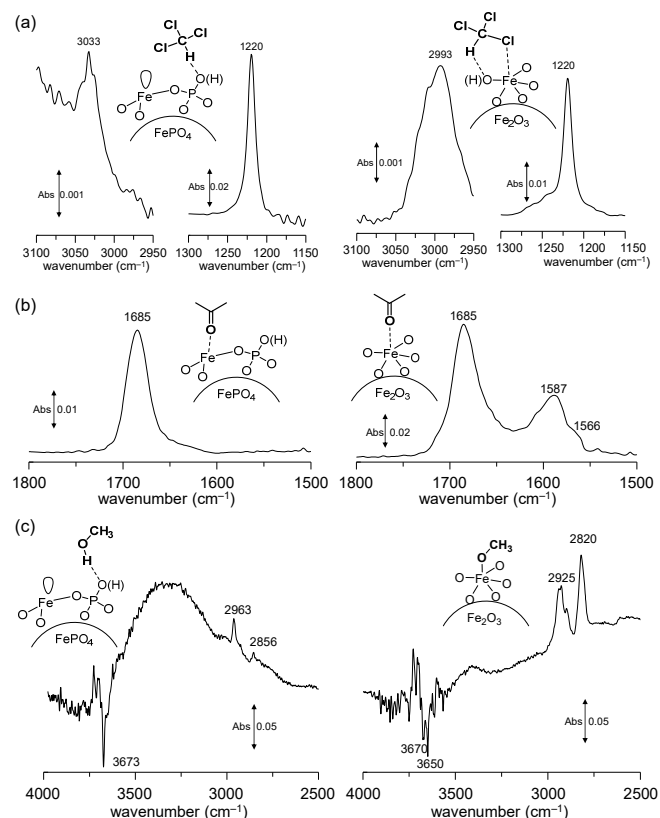


Fig. 10 Difference IR spectra for (a) chloroform-, (b) acetone-, and (c) MeOH-adsorbed FePO₄-MA (left) and Fe₂O₃ (right) at 25 °C.

and Fe₂O₃ were estimated from the intensities of the band around 1446 cm⁻¹ to be 13 μmol g⁻¹ and 50 μmol g⁻¹, respectively. For the activation of CH₄ by [Al₂O₂]⁺, the strong acidity of the aluminum site enables the heterolytic cleavage of the C–H bond of CH₄ via PCET.⁶⁶ In the present catalysis, the strong Lewis acid site of the tetrahedral Fe³⁺ species likely plays an important role in the activation of CH₄. The basicity was also confirmed by IR spectroscopy with adsorbed CHCl₃ (Fig. 10(a)). Although the band due to the C–H stretching mode of the CHCl₃ molecule was observed at 3033 cm⁻¹ and did not shift in comparison with the original band (3034 cm⁻¹) in the case of

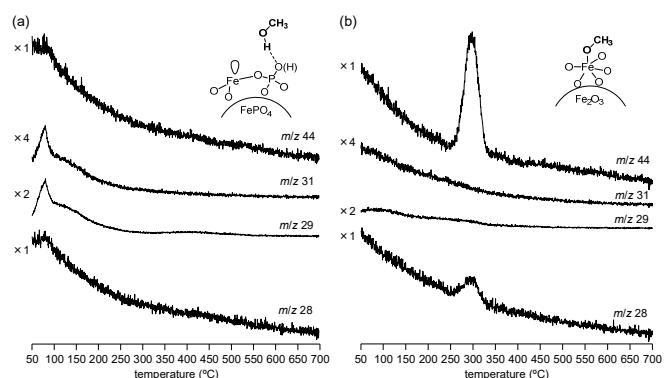


Fig. 11 Mass spectra during temperature-programmed reaction measurement using MeOH-adsorbed (a) $\text{FePO}_4\text{-MA}$ and (b) Fe_2O_3 in stream of He.

$\text{FePO}_4\text{-MA}$, there was a significant red-shift from 3034 cm^{-1} to 2993 cm^{-1} in the case of Fe_2O_3 ; therefore, FePO_4 has much weaker base sites on the surface than Fe_2O_3 .^{44,68,69} Fe_2O_3 exhibited weak and broad shoulder bands around 1250 cm^{-1} , which were ascribed to $\delta(\text{Cl-C-H})$ for the CHCl_3 molecules due to the interaction of the acidic hydrogen and chlorine atoms with the basic oxygen and Lewis acid sites, respectively; however, no such bands were observed for $\text{FePO}_4\text{-MA}$.⁶⁸

Such a difference in the acid-base properties between $\text{FePO}_4\text{-MA}$ and Fe_2O_3 has a strong effect on the interaction with carbonyl compounds and alcohols. It is difficult to use pure HCHO as an adsorbate; therefore, acetone and MeOH were used as model probe molecules. The interaction of acetone with $\text{FePO}_4\text{-MA}$ was confirmed (Fig. 10(b)), and one strong C=O stretching band of acetone adsorbed on $\text{FePO}_4\text{-MA}$ was observed at a lower wavenumber (1685 cm^{-1}) than those of acetone in the gas phase (1731 cm^{-1}) and CePO_4 (1699 cm^{-1}).⁴⁴ On the other hand, the IR spectrum of acetone adsorbed on Fe_2O_3 exhibited bands around $1580\text{--}1550\text{ cm}^{-1}$ assignable to condensed species in addition to a band around 1685 cm^{-1} due to acetone molecules coordinated to Lewis acid sites.^{44,70,71} The $\nu(\text{C=O})$ band of adsorbed condensed species would overlap with a band around 1685 cm^{-1} due to acetone molecules coordinated to Lewis acid sites. All these results indicate that the uniform Lewis acid sites on $\text{FePO}_4\text{-MA}$ without base sites do not promote aldol condensation. The IR spectra for samples with adsorbed MeOH as a probe oxygenate were confirmed (Fig. 10(c)). In the case of $\text{FePO}_4\text{-MA}$, broad bands between 3000 and 3500 cm^{-1} appeared with negative $\nu(\text{O-H})$ bands, and the bands at 2963 and 2856 cm^{-1} were assignable to the asymmetric and symmetric CH_3 stretching modes of molecularly adsorbed MeOH via hydrogen bonds. These results are consistent with previous reports for the non-dissociative adsorption of MeOH on metal oxides and CePO_4 .^{44,72} In contrast, bands were observed at 2925 and 2820 cm^{-1} , which were assignable to $\nu_{\text{as}}(\text{CH}_3)$ and $\nu_{\text{s}}(\text{CH}_3)$ of methoxide species, respectively.^{44,73} These results indicate that FePO_4 without base sites has only weak interaction with MeOH, in sharp contrast to basic Fe_2O_3 , and the similar interaction of HCHO with catalysts may be observed because of its lower $\text{p}K_{\text{a}}$ value (13.29) than MeOH (15.5).⁷⁴

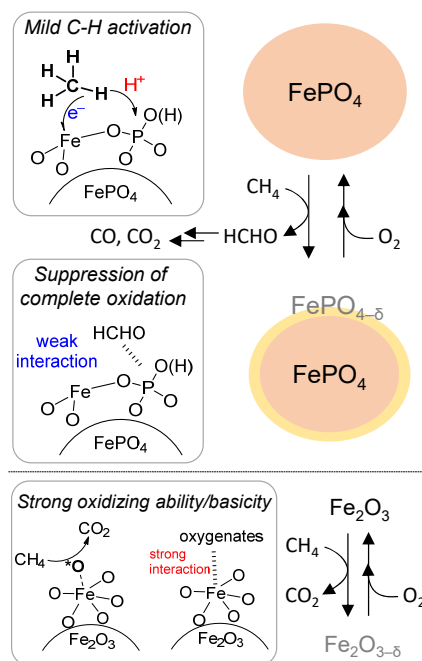


Fig. 12 Proposed reaction mechanism for oxidation of CH_4 over FePO_4 into HCHO with O_2 using $\text{FePO}_4\text{-MA}$ and complete oxidation of CH_4 over Fe_2O_3 into CO_2 with O_2 using Fe_2O_3 .

The temperature-programmed reaction of Fe adsorbed MeOH species in a stream of He was investigated by monitoring the mass spectrum of each product to confirm differences in reactivity between MeOH-adsorbed $\text{FePO}_4\text{-MA}$ and Fe_2O_3 (Fig. 11). The molecularly adsorbed MeOH on $\text{FePO}_4\text{-MA}$ desorbed around $50\text{--}100\text{ }^\circ\text{C}$ as MeOH ($m/z\ 31$) and/or HCHO ($m/z\ 29$), which could possibly be assigned to a fragment peak of MeOH) without significant formation of CO_2 ($m/z\ 44$) or CO ($m/z\ 28$). On the other hand, only the strong desorption peaks due to CO_2 and CO were observed around $250\text{--}300\text{ }^\circ\text{C}$ for the methoxide species adsorbed on Fe_2O_3 , which indicates that such a weak interaction of FePO_4 with oxygenates (e.g., HCHO) contributes to suppression of the complete oxidation of oxygenates into CO_2 , despite its much poorer oxidizing ability than Fe_2O_3 . On the basis of all these results, we propose a possible reaction mechanism for CH_4 oxidation over FePO_4 (Fig. 12). First, CH_4 is oxidized on the FePO_4 surface to produce HCHO and partially reduced FePO_{4-5} , and this step is the rate-determining step. FePO_{4-5} is rapidly oxidized with O_2 to FePO_4 , thereby establishing the catalytic cycle. FePO_4 with uniform Lewis acid sites and weakly basic sites contributes to the specific C-H activation and the weak interaction of FePO_4 with oxygenates (e.g., HCHO), which results in the selective direct oxidation of CH_4 into HCHO.

Conclusions

In summary, various crystalline iron-based phosphate and oxide catalysts were synthesized by the sol-gel method using malic acid or aspartic acid, and their catalytic properties were systematically investigated for the oxidation of CH_4 with O_2 as the sole oxidant. Among these catalysts, trigonal FePO_4

nanoparticles (FePO₄-MA) exhibited the highest catalytic performance for the direct oxidation of CH₄ into HCHO. The Fe/P molar ratios for iron phosphates strongly affected the catalytic activity and selectivity toward the production of HCHO. Although the redox cycle between FePO₄ and Fe₂P₂O₇ was observed during reaction of the reductants (H₂ and CH₄) and oxidant (O₂) based on the TG-DTA, XRD, and temperature-programmed reaction results for FePO₄-MA, mechanistic studies including the catalyst effect, kinetics, and pulse reaction experiments suggested that this redox cycle was not involved during catalysis under steady-state conditions, and that the oxidation of CH₄ proceeds on the FePO₄ surface with the structure preservation of bulk FePO₄. IR spectroscopy measurements of FePO₄ and Fe₂O₃ with adsorbed probe molecules indicated that the weak interaction of FePO₄ containing uniform Lewis acid sites and weak basic sites with C₁-oxygenates likely suppresses subsequent oxidation into CO₂. Such a C–H activation mode (formally PCET) and the weak basic properties of FePO₄ result in high catalytic performance for the selective direct oxidation of CH₄ into HCHO. However, the possibility of FePO₄-MA subsurface reduction/oxidation during the reaction cannot be fully excluded by the present results. In this context, further investigation on the real-working state of FePO₄ during the catalytic oxidation of CH₄ to oxygenates is required, and operando spectroscopic techniques definitely help us to understand detailed dynamics of FePO₄ during the catalysis.⁷⁵

This study suggests the importance of the effect of phosphate units on the selective activation of CH₄ into the desired products. Further catalyst design and/or fine-control of the metal phosphate synthesis could lead to the development of efficient catalysts for direct CH₄ transformation reactions that are in sharp contrast to metal oxides. While the low HCHO yield of FePO₄-MA should be improved, this approach is a promising strategy for the establishment of selective CH₄ oxidation by control of the surface redox and acid-base properties of heterogeneous catalysts.

Author Contributions

A.M., H.T., and K.K. designed the experiments, performed the experimental investigation, and conducted data analyses. K.K. wrote the paper. The draft was reviewed by A.M., K.K., and M.H.

Conflicts of interest

There are no conflicts of interest to declare.

Acknowledgements

This study was funded in part by a Grant-in-Aid (18H01786) for Scientific Research from the Japan Society for the Promotion of Science (JSPS), and the PRESTO (JPMJPR15S3) and CREST (JPMJCR16P3) programs of the Japan Science and Technology Agency (JST), the Tokuyama Science Foundation, and the "Creation of Life Innovative Materials for Interdisciplinary and

International Researcher Development" program of the Japan Ministry of Education, Culture, Sports, Science and Technology (MEXT).

Notes and references

- 1 D. Saha, H. A. Grappe, A. Chakraborty and G. Orkoulas, *Chem. Rev.*, 2016, **116**, 11436–11499.
- 2 R. Horn and R. Schlögl, *Catal. Lett.*, 2015, **145**, 23–39.
- 3 A. Abdulrasheed, A. A. Jalil, Y. Gambo, M. Ibrahim, H. U. Hambali and M. Y. Shahul Hamid, *Renew. Sust. Energ. Rev.* 2019, **108**, 175–193.
- 4 C. Hammond, S. Conrad and I. Hermans, *ChemSusChem*, 2012, **5**, 1668–1686.
- 5 K. Otsuka and Y. Wang, *Appl. Catal. A: Gen.*, 2001, **222**, 145–161.
- 6 A. I. Olivos-Suarez, Á. Szécsényi, E. J. M. Hensen, J. Ruiz-Martinez, E. A. Pidko and J. Gascon, *ACS Catal.*, 2016, **6**, 2965–2981.
- 7 M. Ravi, M. Ranocchiaro and J. A. van Bokhoven, *Angew. Chem. Int. Ed.*, 2017, **56**, 16464–16483.
- 8 A. V. Vekki and S. T. Marakaev, *Russ. J. Appl. Chem.*, 2009, **82**, 521–536.
- 9 A. H. Bagherzadeh Mostaghimi, T. A. Al-Attas, M. G. Kibria and S. Siahrostami, *J. Mater. Chem. A*, 2020, **8**, 15575–15590.
- 10 S. Ogo and Y. Sekine, *Chem. Rec.*, 2017, **17**, 726–738.
- 11 I. Vollmer, I. Yarulina, F. Kapteijn and J. Gascon, *ChemCatChem*, 2018, **11**, 39–52.
- 12 K. Sun, D. M. Ginosar, T. He, Y. Zhang, M. Fan and R. Chen, *Ind. Eng. Chem. Res.*, 2018, **57**, 1768–1789.
- 13 H. Schwarz, *Angew. Chem. Int. Ed.*, 2011, **50**, 10096–10115.
- 14 M. H. Mahyuddin, Y. Shiota and K. Yoshizawa, *Catal. Sci. Technol.*, 2019, **9**, 1744–1768.
- 15 Z. Jin, L. Wang, E. Zuidema, K. Mondal, M. Zhang, J. Zhang, C. Wang, X. Meng and H. Yang, *Science*, 2020, **367**, 193–197.
- 16 P. Xiao, Y.; Wang, T. Nishitoba, J. N. Kondo and T. Yokoi, *Chem. Commun.*, 2019, **55**, 2896–2899.
- 17 C. Hammond, M. M. Forde, M. H. Ab Rahim, A. Thetford, Q. He, R. L. Jenkins, N. Dimitratos, J. A. Lopez-Sanchez, N. F. Dummer, D. M. Murphy, A. F. Carley, S. H. Taylor, D. J. Willock, E. E. Stangland, J. Kang, H. Hagen, C. J. Kiely and G. J. Hutchings, *Angew. Chem. Int. Ed.*, 2012, **51**, 5129–5133.
- 18 B. E. R. Snyder, M. L. Bols, R. A. Schoonheydt, B. F. Sels and E. I. Solomon, *Chem. Rev.*, 2018, **118**, 2718–2768.
- 19 P. Schwach, M. G. Willinger, A. Trunschke and R. Schlögl, *Angew. Chem. Int. Ed.*, 2013, **52**, 11381–11384.
- 20 J. H. Lunsford, *Angew. Chem. Int. Ed. Engl.*, 1995, **34**, 970–980.
- 21 B. P. C. Hereijgers and B. M. Weckhuysen, *ChemSusChem*, 2009, **2**, 743–748.
- 22 M. Bugnola, R. Carmieli and R. Neumann, *ACS Catal.*, 2018, **8**, 3232–3236.
- 23 B. Wu, R. Yang, L. Shi, T. Lin, X. Yu, M. Huang, K. Gong, F. Sun, Z. Jiang, S. Li, L. Zhong and Y. Sun, *Chem. Commun.*, 2020, **56**, 14677–14680.
- 24 K. Harrath, X. Yu, H. Xiao and J. Li, *ACS Catal.*, 2019, **9**, 8903–8909.
- 25 C. Williams, J. H. Carter, N. F. Dummer, Y. K. Chow, D. J. Morgan, S. Yacob, P. Serna, D. J. Willock, R. J. Meyer, S. H. Taylor and G. J. Hutchings, *ACS Catal.*, 2018, **8**, 2567–2576.
- 26 J. Baek, B. Rungtaweeworanit, X. Pei, M. Park, S. C. Fakra, Y. S. Liu, R. Matheu, S. A. Alshmiri, S. Alshehri, C. A. Trickett, G. A. Somorjai and O. M. Yaghi, *J. Am. Chem. Soc.*, 2018, **140**, 18208–18216.
- 27 T. Ikuno, J. Zheng, A. Vjunov, M. Sanchez-Sanchez, M. A. Ortuno, D. R. Pahls, J. L. Fulton, D. M. Camaioni, Z. Li, D. Ray, B. L. Mehdi, N. D. Browning, O. K. Farha, J. T. Hupp, C. J.

- Cramer, L. Gagliardi and J. A. Lercher, *J. Am. Chem. Soc.*, 2017, **139**, 10294–10301.
- 28 T. Ohno and J. B. Moffat, *Catal. Lett.*, 1992, **16**, 181–190.
- 29 A. V. Annapragada and E. Gulari, *J. Catal.*, 1990, **123**, 130–146.
- 30 A. Sato, S. Ogo, K. Kamata, Y. Takeno, T. Yabe, T. Yamamoto, S. Matsumura, M. Hara and Y. Sekine, *Chem. Commun.*, 2019, **55**, 4019–4022.
- 31 V. Paunovic, G. Zichittella, M. Moser, A. P. Amrute and J. Perez-Ramirez, *Nat. Chem.*, 2016, **8**, 803–809.
- 32 G. Zichittella, V. Paunović, A. P. Amrute and J. Pérez-Ramírez, *ACS Catal.*, 2017, **7**, 1805–1817.
- 33 R. Wang, R. Lin, Y. Ding, J. Liu, J. Wang and T. Zhang, *Appl. Catal. A: Gen.*, 2013, **453**, 235–243.
- 34 Y. Wang and K. Otsuka, *J. Catal.*, 1995, **155**, 256–267.
- 35 X. Wang, Y. Wang, Q. Tang, Q. Guo, Q. Zhang and H. Wan, *J. Catal.*, 2003, **217**, 457–467.
- 36 Y. Wang, X. Wang, Z. Su, Q. Guo, Q. Tang, Q. Zhang and H. Wan, *Catal. Today*, 2004, **93–95**, 155–161.
- 37 V. D. B. C. Dasireddy, D. Hanzel, K. Bharuth-Ram, B. Likozar, *RSC Adv.* 2019, **9**, 30989–31003.
- 38 G. O. Alptekin, A. M. Herring, D. L. Williamson, T. R. Ohno and R. L. McCormick, *J. Catal.*, 1999, **181**, 104–112.
- 39 Y. Wang and K. Otsuka, *J. Mol. Catal. A: Chem.*, 1996, **111**, 341–356.
- 40 Y. Wang and K. Otsuka, *J. Chem. Soc., Faraday Trans.*, 1995, **91**, 3953–3961.
- 41 M. Lopez Granados and E. E. Wolf, *Appl. Catal. A: Gen.*, 1995, **131**, 263–281.
- 42 V. Gomonaj and H. Toulhoat, *ACS Catal.*, 2018, **8**, 8263–8272.
- 43 J.-M. M. Millet, *Catal. Rev. Sci. Eng.*, 1998, **40**, 1–38.
- 44 S. Kanai, I. Nagahara, Y. Kita, K. Kamata and M. Hara, *Chem. Sci.*, 2017, **8**, 3146–3153.
- 45 K. Sugahara, K. Kamata, S. Muratsugu and M. Hara, *ACS Omega*, 2017, **2**, 1608–1616.
- 46 S. Shibata, K. Sugahara, K. Kamata and M. Hara, *Chem. Commun.*, 2018, **54**, 6772–6775.
- 47 K. Kamata, K. Sugahara, Y. Kato, S. Muratsugu, Y. Kumagai, F. Oba and M. Hara, *ACS Appl. Mater. Interfaces*, 2018, **10**, 23792–23801.
- 48 Y. Sugawara, K. Kamata and T. Yamaguchi, *ACS Appl. Energy Mater.*, 2019, **2**, 956–960.
- 49 K. Kamata, *Bull. Chem. Soc. Jpn.*, 2019, **92**, 133–151.
- 50 Y. Sugawara, T. Hihara, G. M. Anilkumar, K. Kamata and T. Yamaguchi, *Sustain. Energy Fuels*, 2021, **5**, 1374–1378.
- 51 S. Shibata, K. Kamata and M. Hara, *Catal. Sci. Technol.*, 2021, **11**, 2369–2373.
- 52 Y. Yamaguchi, R. Aono, E. Hayashi, K. Kamata and M. Hara, *ACS Appl. Mater. Interfaces*, 2020, **12**, 36004–36013.
- 53 G. N. Kastanas, G. A. Tsigdinos and J. Schwank, *Appl. Catal.*, 1988, **44**, 33–51.
- 54 S. K. J. B. Moffat, *J. Chem. Soc., Chem. Commun.*, 1987, 1663–1664.
- 55 Y.-m. Zhu, Z.-w. Ruan, S.-z. Tang and V. Thangadurai, *Ionics*, 2014, **20**, 1501–1510.
- 56 K. A. Ross, M. M. Bordelon, G. Terho and J. R. Neilson, *Phys. Rev. B*, 2015, **92**, 134419.
- 57 L. K. Elbouaanani, B. Malaman, R. Gérardin and M. Ijjaali, *J. Solid State Chem.*, 2002, **163**, 412–420.
- 58 R. M. Cornell and U. Schwertmann, *The Iron Oxides: Structure, Properties, Reactions, Occurrences and Uses*, Second Edition, Wiley-VCH, Weinheim, 2003.
- 59 A. M. Beale and G. Sankar, *J. Mater. Chem.*, 2002, **12**, 3064–3072.
- 60 Z. C. Shi, A. Attia, W. L. Ye, Q. Wang, Y. X. Li and Y. Yang, *Electrochim Acta*, 2008, **53**, 2665–2673.
- 61 R. Lin, A. P. Amrute, F. Krumeich, K. Lázár, R. Hauert, M. Yulikov and J. Pérez-Ramírez, *CrystEngComm*, 2016, **18**, 3174–3185.
- 62 K. Nakajima, Y. Baba, R. Noma, M. Kitano, J. N. Kondo, S. Hayashi and M. Hara, *J. Am. Chem. Soc.*, 2011, **133**, 4224–4227.
- 63 T. Stefanidis and A. G. Nord, *Z. Kristallogr.*, 1982, **159**, 255–264.
- 64 J.-M. M. Millet, J. C. Vedrine and G. Hecquet, *Stud. Surf. Sci. Catal.*, 1990, **55**, 833–841.
- 65 D. R. Weinberg, C. J. Gagliardi, J. F. Hull, C. F. Murphy, C. A. Kent, B. C. Westlake, A. Paul, D. H. Ess, D. G. McCafferty and T. J. Meyer, *Chem. Rev.*, 2012, **112**, 4016–4093.
- 66 J. Li, S. Zhou, J. Zhang, M. Schlangen, T. Weiske, D. Usharani, S. Shaik and H. Schwarz, *J. Am. Chem. Soc.*, 2016, **138**, 7973–7981.
- 67 L. Yue, J. Li, S. Zhou, X. Sun, M. Schlangen, S. Shaik and H. Schwarz, *Angew. Chem. Int. Ed.*, 2017, **56**, 10219–10223.
- 68 T. Komanoya, K. Nakajima, M. Kitano and M. Hara, *J. Phys. Chem. C*, 2015, **119**, 26540–26546.
- 69 J. Xie, M. Huang and S. Kaliaguine, *React. Kinet. Catal. Lett.*, 1996, **58**, 217–227.
- 70 M. I. Zaki, M. A. Hasan and L. Pasupulety, *Langmuir*, 2001, **17**, 768–774.
- 71 M. I. Zaki, M. A. Hasan, F. A. Al-Sagheer and L. Pasupulety, *Langmuir*, 2000, **16**, 430–436.
- 72 Z. Martinez-Ramirez, G. A. Flores-Escamilla, G. S. Berumen-Espana, S. A. Jimenez-Lam, B. E. Handy, M. G. Cardenas-Galindo, A. G. Sarmiento-Lopez and J. C. Fierro-Gonzalez, *Appl. Catal. A: Gen.*, 2015, **502**, 254–261.
- 73 Z. Wu, M. Li, D. R. Mullins and S. H. Overbury, *ACS Catal.*, 2012, **2**, 2224–2234.
- 74 G. B. Barlin and D. D. Perrin, *Q. Rev. Chem. Soc.*, 1966, **20**, 75–101.
- 75 G. Zichittella, Dr. Y. Polyhach, R. Tschaggelar, G. Jeschke and J. Pérez-Ramírez, *Angew. Chem. Int. Ed.*, 2021, **60**, 3596–3602.